Journal of
Applied Crystallography
ISSN 0021-8898
Editor: **Anke R. Pyzalla**

Local atomic structure in tetragonal pure ZrO_2 nanopowders

Leandro M. Acuña, Diego G. Lamas, Rodolfo O. Fuentes, Ismael O. Fábregas, Márcia C. A. Fantini, Aldo F. Craievich and Rogério J. Prado

J. Appl. Cryst. (2010). **43**, 227–236

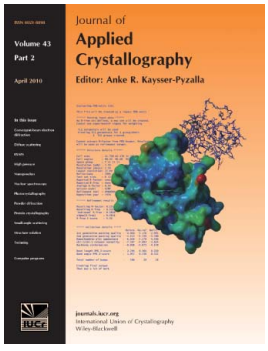

Journal of
Applied Crystallography
ISSN 0021-8898

Received 11 July 2009
Accepted 21 December 2009

Local atomic structure in tetragonal pure ZrO_2 nanopowders

Leandro M. Acuña,[a] Diego G. Lamas,[a]* Rodolfo O. Fuentes,[a] Ismael O. Fábregas,[a] Márcia C. A. Fantini,[b] Aldo F. Craievich[b] and Rogério J. Prado[c]

[a]CINSO (Centro de Investigaciones en Sólidos), CITEFA-CONICET, J. B. de La Salle 4397, (B1603ALO) Villa Martelli, Provincia de Buenos Aires, Argentina, [b]Instituto de Física, Universidade de São Paulo, Travessa R da Rua do Matão, No. 187, Cidade Universitaria, 05508-900, São Paulo, Brazil, and [c]Instituto de Física, Universidade Federal de Mato Grosso (UFMT), Avenida Fernando Corrêa s/n, 78060-900, Cuiabá, MT, Brazil. Correspondence e-mail: dlamas@citefa.gov.ar

The local atomic structures around the Zr atom of pure (undoped) ZrO_2 nanopowders with different average crystallite sizes, ranging from 7 to 40 nm, have been investigated. The nanopowders were synthesized by different wet-chemical routes, but all exhibit the high-temperature tetragonal phase stabilized at room temperature, as established by synchrotron radiation X-ray diffraction. The extended X-ray absorption fine structure (EXAFS) technique was applied to analyze the local structure around the Zr atoms. Several authors have studied this system using the EXAFS technique without obtaining a good agreement between crystallographic and EXAFS data. In this work, it is shown that the local structure of ZrO_2 nanopowders can be described by a model consisting of two oxygen subshells (4 + 4 atoms) with different Zr—O distances, in agreement with those independently determined by X-ray diffraction. However, the EXAFS study shows that the second oxygen subshell exhibits a Debye–Waller (DW) parameter much higher than that of the first oxygen subshell, a result that cannot be explained by the crystallographic model accepted for the tetragonal phase of zirconia-based materials. However, as proposed by other authors, the difference in the DW parameters between the two oxygen subshells around the Zr atoms can be explained by the existence of oxygen displacements perpendicular to the **z** direction; these mainly affect the second oxygen subshell because of the directional character of the EXAFS DW parameter, in contradiction to the crystallographic value. It is also established that this model is similar to another model having three oxygen subshells, with a 4 + 2 + 2 distribution of atoms, with only one DW parameter for all oxygen subshells. Both models are in good agreement with the crystal structure determined by X-ray diffraction experiments.

1. Introduction

ZrO_2-based materials are widely studied because of their excellent electrical and mechanical properties (Nowotny, 1994; Lee & Rainforth, 1994; Garvie *et al.*, 1975; Juárez *et al.*, 1999). The high ionic conductivity through oxygen vacancies at high temperature makes these materials suitable to be used as electrolyte in solid-oxide fuel cells, oxygen sensors and oxygen pumps. Pure ZrO_2 exhibits three phases at normal atmospheric pressure with increasing temperature: monoclinic (space group $P2_1/c$) from room temperature to 1443 K, tetragonal ($P4_2/nmc$) from 1443 to 2643 K and cubic ($Fm\bar{3}m$) from 2643 to 3023 K. The two high-temperature phases are the most important for practical applications. The properties of ZrO_2-based materials strongly depend on their type of phase, average crystal structure and local atomic order.

The tetragonal phase of ZrO_2 is not thermodynamically stable at room temperature, but it can be retained in a metastable condition in nanocrystalline powders with crystallite sizes smaller than a certain critical size, typically between 20 and 50 nm (Juárez *et al.*, 1999; Garvie, 1965, 1978; Lascalea *et al.*, 2001).

Even though ZrO_2-based compounds have been widely studied, numerous discrepancies remain regarding the underlying mechanisms governing the retention of the tetragonal phase. For example, the role of oxygen vacancies is controversial. In this scenario, the understanding of the relationship between the average crystal structure and the local atomic order is crucial and, therefore, extended X-ray

Table 1
Overview of some published work on ZrO_2-based materials.

N: coordination number; *R*: Zr—O distance; σ^2: Debye–Waller parameter; E_0: correction to energy threshold. It can be seen that there are mainly two models used for fitting the first oxygen shell of the Zr atom in samples that exhibit the tetragonal phase.

Author	Composition	*N*	*R* (Å)	σ^2 (10^{-3} Å^2)	E_0 (eV)
Li *et al.* (1993*a*,*b*, 1994)	ZrO_2–3 mol%	4	2.10	3.4	0
	Y_2O_3	4	2.33	9.0	0
	ZrO_2–25 mol%	4	2.10	4.0	Not reported
	CeO_2	4	2.34	11.5	Not reported
Chadwick *et al.* (2001)	*t*-ZrO_2	4	2.10	4.5	Not reported
		4	2.31	14.0	Not reported
	ZrO_2–8 mol%	4	2.10	6.5	Not reported
	Y_2O_3	4	2.32	18.0	Not reported
Lemaux *et al.* (2001)	ZrO_2–1 mol%	4	2.10	−0.7	−1.1
	Y_2O_3	4	2.27	5.1	3.6
	ZrO_2–50 mol%	4	2.11	0.0	−3.4
	CeO_2	4	2.23	3.0	4.7
Vlaic *et al.* (1999)	ZrO_2–50 mol%	4	2.12	6.1	0.0
	CeO_2	2	2.32	6.1	0.0
Fornasiero *et al.* (1999)	ZrO_2–60 mol%	5	2.13	5.9	3.5
	CeO_2	2	2.32	5.9	3.5
Kriventsov *et al.* (2001)	$Fe_{0.05}/ZrO_2$	4.1	2.13	5	Not reported
	composite	2.2	2.32	5	Not reported
	$Fe_{0.1}/ZrO_2$	3.9	2.12	5	Not reported
	composite	2.5	2.29	5	Not reported

absorption fine structure (EXAFS) spectroscopy could give valuable information.

There is no general consensus for the local atomic order of ZrO_2-based materials. For example, although eightfold coordination of Zr is generally assumed for the tetragonal phase (Lee & Rainforth, 1994; Juárez *et al.*, 1999), a sixfold coordination model was found by EXAFS in ZrO_2 nanocrystals doped with CeO_2 or Fe/ZrO_2 composites (Vlaic *et al.*, 1999; Fornasiero *et al.*, 1999; Kriventsov *et al.*, 2001). This is in strong contradiction to the crystal structure of the tetragonal phase clearly established by a number of X-ray diffraction experiments.

Vlaic *et al.* (1999) found a 4 + 2 + 2 model for the local structure of the Zr atom in tetragonal ZrO_2–20 mol% CeO_2 and a 4 + 2 model for compositions of 50 and 60 mol% CeO_2. In order to explain the low coordination number in the 50 mol% CeO_2 sample, Fornasiero *et al.* (1999) proposed a 4 + 2 + 2 model in which the third oxygen subshell is at a distance further than 2.60 Å from the central Zr atom. They argued that this subshell therefore does not contribute significantly to the EXAFS signal and cannot be detected.

On the other hand, other authors (Li *et al.*, 1993*a*,*b*, 1994; Chadwick *et al.*, 2001; Lemaux *et al.*, 2001) proposed a 4 + 4 model for the Zr—O bond in tetragonal ZrO_2, pure or doped with trivalent or tetravalent cations. In particular, Lemaux *et al.* (2001) proposed a 4 + 4 model for ZrO_2–50 mol% CeO_2 materials, with an important anharmonicity of the distance distribution of the second Zr—O bond R_2. Table 1 is a brief overview of the results of these studies.

In the present work, we used the EXAFS technique to analyze the local atomic order in nanocrystalline undoped ZrO_2 powders exhibiting the tetragonal phase. These local structure arrangements were compared with those determined from synchrotron radiation X-ray diffraction (SR-XRD) experiments in order to establish a consistent model for the Zr—O bonding that agrees with the crystal structure generally accepted for the tetragonal phase. The influence of the crystallite size on the local atomic structure around Zr atoms was also investigated. Both an experimental standard and a theoretical model were applied to fit the amplitude and phase of the EXAFS signal. We will show that, surprisingly, the local order of Zr expected from the crystal structure widely accepted for the tetragonal phase (space group $P4_2/nmc$) does not fit our EXAFS data. For this reason, different models for the first oxygen shell around Zr were tested, checking the fit quality and their consistency with SR-XRD data.

To our knowledge, there are no other papers reporting systematic and comparative studies on the reliability of all the models considered in this work for the local atomic order around Zr atoms of the tetragonal phase in pure ZrO_2. Up to the present time, different authors have elected models without considering other possibilities and, in many cases, without comparing the results of their EXAFS analysis with the crystal structure that can be investigated by XRD experiments. Our goal was to find a structure that explains the local order of tetragonal pure ZrO_2 nanopowders and, at the same time, matches their crystallographic long-range order determined by SR-XRD experiments, as well as to uncover new information about the disorder of the O atoms in nanostructured zirconia.

2. Experimental procedure

2.1. Synthesis of nanocrystalline pure ZrO_2 powders

ZrO_2 nanopowders were synthesized by different stoichiometric gel-combustion processes using glycine, lysine or alanine (Merck, USA, 99%) as fuels (Lamas *et al.*, 2006).

$ZrO(NO_3)_2{\cdot}6H_2O$ (Fluka, USA, 99%) and fuel were dissolved in distilled water in an amount corresponding to 0.02 mol of final product. The resulting solution was concentrated by thermal evaporation using a hot-plate at 473 K until a viscous white gel was obtained. The gel was further heated until it burned out as a result of a moderated exothermic reaction. The system remained homogeneous during the whole process and no precipitation was observed.

The as-reacted materials synthesized using glycine and alanine fuels were calcined in air at 773 K for 1 h, while that obtained by the lysine route was calcined at 873 K for 1 h. These calcination temperatures were selected in order to achieve the full retention of the tetragonal phase. These nanocrystalline powders exhibited average crystallite sizes (derived from SR-XRD analysis) of 7, 9 and 14 nm. Additionally, a nanocrystalline powder with an average crystallite size of 41 nm was prepared by a sol-gel route in which hydrolysis and condensation of zirconium *n*-butoxide occur.

2.2. Synchrotron radiation X-ray diffraction analysis

The nature of the crystalline phases in ZrO_2 nanopowders and their average crystallite size were determined by SR-XRD. These experiments were carried out at the D10B-XPD beamline of the Brazilian Synchrotron Light Laboratory (LNLS, Campinas, Brazil) (Furlan Ferreira *et al.*, 2006).

The X-ray wavelength for SR-XRD measurements was set at 1.5500 Å. A low-resolution (high-intensity) configuration, without crystal analyzer, was selected. This high photon flux setup is appropriate for the discrimination between the tetragonal and the cubic phases and for the precise determination of the z coordinate of the O^{2-} anions in the tetragonal phase (Lamas *et al.*, 2005, 2006).

The average crystallite size of the samples was determined from the broadening of the (111) Bragg peak by means of the Scherrer equation. Rietveld refinements of SR-XRD data assuming the crystal structure widely accepted for the tetragonal phase (space group $P4_2/nmc$ with Zr^{4+} cations and O^{2-} anions in the 2*a* and 4*d* positions, respectively) were performed in order to determine the lattice parameters. The fractional z coordinate of the O atom in the asymmetric unit of the tetragonal unit cell, z(O), was obtained from the ratio of the measured integrated intensities of the (111) and (112) Bragg peaks (Lamas *et al.*, 2005, 2006).

2.3. Extended X-ray absorption fine structure analysis

EXAFS measurements at the Zr *K*-edge were carried out at the D04B-XAFS1 beamline of the LNLS (Tolentino *et al.*, 1998) in transmission mode. The energy of the X-ray incident radiation was controlled with an Si(220) monochromator. The energy range was 17 900–18 900 eV. A Zr metallic foil was used to calibrate the Zr *K*-edge energy. Data were collected at room temperature using energy steps of 2 eV in the range 17 900–18 400 eV and 4 eV for higher energies. The integration time was 4 and 12 s, respectively. The powder samples were suspended in 2-propanol and deposited on Millipore membranes. The thicknesses were adjusted to obtain a total absorption above the edge of 1.5.

Data reduction was performed using the *WinXas* code (Ressler, 1998) following the procedure described elsewhere (Fábregas *et al.*, 2006, 2008). Both pre- and post-edge backgrounds were subtracted from the raw data. A linear fit of the absorption signal was subtracted from the experimental data for the pre-edge region (background correction) and a fifth-order polynomial was used for the post-edge removal. The spectra were normalized to unit step height.

EXAFS data analysis was based on two procedures: (i) use of an experimental standard to obtain amplitude and phase parameters to fit the first coordination shell of the Zr atom, and (ii) theoretical calculations that give parameters to fit the first and second coordination shells. The models used for fitting EXAFS data of the first coordination shell of the Zr atom are summarized in Table 2.

2.3.1. Analysis with experimental standard. $BaZrO_3$ was used as the standard compound (six O atoms at 2.09 Å from zirconium) to obtain the experimental scattering amplitude and phase required for EXAFS data analysis of Zr—O bonds in the first shell around the Zr cation in pure ZrO_2. The DW parameters were set equal to zero. Hence, the values of the adjustable disorder parameters presented hereinafter represent the variations with respect to those of the reference compound. Data analysis was performed using the *WinXas* code (Ressler, 1998).

Table 2
Models for the local structure around Zr for tetragonal ZrO_2 nanopowders.

N: coordination number; σ^2: Debye–Waller parameter; E_0: correction to energy threshold. The subscripts 1, 2 and 3 refer to the first, second and third O subshell, respectively. (f): fixed; (v): variable. In all cases, both Zr—O distances (R_i) were varied

Model	Fitting conditions		
1†	$N_1 = N_2 = 4$ (f)	$\sigma_1^2 = \sigma_2^2$ (v)	$E_{01} = E_{02}$ (v)
2	$N_1 = N_2 = 4$ (f)	$\sigma_1^2 \neq \sigma_2^2$ (v)	$E_{01} = E_{02}$ (v)
3	N_1, N_2 (v)	$\sigma_1^2 = \sigma_2^2$ (v)	$E_{01} = E_{02}$ (v)
4	$N_1 = 4$, $N_2 = 2$, $N_3 = 2$ (f)	$\sigma_1^2 = \sigma_2^2 = \sigma_3^2$ (v)	$E_{01} = E_{02} = E_{03}$ (v)

† Data derived from the known crystallographic structure (space group $P4_2/nmc$).

The Fourier transform (FT) was calculated from the k^3-weighted EXAFS oscillations in the range k = 3.0–13.3 Å^{-1} (k is the photoelectron wavenumber), and the window of the back FT was R = 1.1–2.3 Å in R space in order to isolate the contribution of the first O shell to the EXAFS signal (R is the conjugated variable of k). For the calculation of the FT, a Gaussian window was set (window parameter = 30) for all analyzed data. The limits of the FT window were selected taking into account the signal-to-noise ratio (S/N) of the EXAFS data (Lee *et al.*, 1981). Fits to the k-weighted back FT were performed.

2.3.2. Analysis with theoretical amplitudes and phases. The theoretical amplitudes and phases were calculated with the *FEFF8* code (Ankudinov *et al.*, 1998). Again, a Gaussian window was used for the calculation of the FT of the k^3-weighted EXAFS signal in the range k = 3.0–13.3 Å^{-1}. The quantitative fitting was performed in R space on the FT of the k^3-weighted oscillation, using the *FEFFIT* code (Newville *et al.*, 1995). We selected the R-space interval from 1.20 to 3.80 Å to include the nearest neighbor (NN) and next nearest neighbor (NNN) contributions. The reduction factor S_0^2 was set equal to unity. The results obtained by this procedure were compared with those determined by using experimental scattering amplitude and phase. Since many models were tested, only the main and relevant results will be presented.

3. Results

3.1. Synchrotron radiation X-ray diffraction

Our SR-XRD study confirmed the retention of the high-temperature tetragonal phase at room temperature for all ZrO_2 samples. Table 3 summarizes the results of the average crystallite size D, the lattice parameters of the tetragonal phase a and c, which are indicated in terms of a pseudo-fluorite unit cell (thus $a \simeq c$), the axial ratio c/a, the fractional

Table 3
Results of the SR-XPD study of tetragonal pure ZrO_2 nanopowders.

D: average crystallite size; *a* and *c*: lattice parameters; *z*(O): fractional *z* coordinate of the O atom in the asymmetrical unit of the tetragonal unit cell; R_1 and R_2: Zr—O distances for the first and second subshells, respectively. SGC denotes the stoichiometric gel-combustion process.

Sample	*D* (nm)	*a* (Å)	*c* (Å)	*c*/*a*	*z*(O)	R_1 (Å)	R_2 (Å)
Pure ZrO_2: SGC – alanine – 773 K	7.0 (3)	5.0921 (4)	5.184 (2)	1.0180 (5)	0.222 (1)	2.137 (3)	2.305 (4)
Pure ZrO_2: SGC – glycine – 773 K	9.0 (5)	5.0897 (4)	5.176 (2)	1.0170 (5)	0.222 (1)	2.135 (3)	2.305 (4)
Pure ZrO_2: SGC – lysine – 873 K	14 (1)	5.0890 (3)	5.185 (1)	1.0189 (3)	0.214 (1)	2.113 (3)	2.332 (3)
Pure ZrO_2: sol-gel – 673 K	41 (4)	5.0807 (3)	5.1637 (6)	1.0163 (2)	0.210 (1)	2.098 (3)	2.339 (3)

coordinate of the O atom in the asymmetric unit of the tetragonal unit cell *z*(O), and the Zr—O distances R_i. The results obtained in this investigation are in good agreement with those reported by Lamas *et al.* (2006) for materials with similar average crystallite sizes.

3.2. EXAFS analysis

In Fig. 1, the k^3-weighted raw EXAFS signals at the Zr *K*-edge, corresponding to all the studied samples, are displayed as functions of *k*. The ordinate axis was shifted in order to better visualize the differences in the spectra. A high S/N in the *k* window from 3 to 13.3 $Å^{-1}$ was obtained in all cases (S/N > 20 over the selected interval). Note the similarity between the EXAFS spectra corresponding to samples with average crystallite size of 7 and 9 nm and, also, between the spectra of the samples with average crystallite sizes of 14 and 41 nm.

Fig. 2 displays the FTs of the EXAFS signal corresponding to several samples with different average crystallite sizes. The peaks between 1.1 and 2.3 Å are related to the contribution of the first oxygen shell around the Zr atoms, while the second band, between 2.3 and 4 Å, contains information related to the Zr–Zr neighbors and O second neighbors. The peak at $R < 1$ Å is due to the low-frequency oscillation in the atomic background, so its elimination by filtering with software tools does not affect the analysis of the *R* range of interest (Koningsberger & Prins, 1988). The second peak decreases for samples with decreasing crystallite size, as is expected for progressively less ordered structures. The EXAFS parameters obtained from each fit are the atomic distance R_i, the DW disorder parameter σ_i^2 and the threshold electron energy shift E_{0i}. The error of the DW parameter was estimated to be 5%, although the uncertainty reported by the *WinXas* code was smaller.

We started our analysis testing the crystallographic model widely accepted for the tetragonal phase. In this model (Model 1) the Zr atoms are surrounded by eight O atoms distributed in two subshells with different distances from the central Zr atom. Both subshells contain the same number of O atoms ($N_1 = N_2 = 4$), and have equivalent DW parameters ($\sigma_1^2 = \sigma_2^2$) and threshold electron energy shifts ($E_{01} = E_{02}$). The goodness of fit (*R* factor) for this model was very poor ($r > 25$), indicating that Model 1 is not adequate to describe the local atomic structure of the nanocrystalline pure ZrO_2 materials studied in this work, in spite of being the widely accepted model for their crystallographic long-range order.

Other models for the local structure around Zr atoms were tested. Model 2 ($N_1 = N_2 = 4$; $\sigma_1^2 \neq \sigma_2^2$; $E_{01} = E_{02}$) is essentially equivalent to Model 1 except for the DW parameters, which are allowed to be different for subshells 1 and 2. Model 3 (N_1, N_2 free; $\sigma_1^2 = \sigma_2^2$; $E_{01} = E_{02}$) is also similar to Model 1, except for N_1 and N_2, which are both free parameters. The EXAFS function derived from these two models (2 and 3) exhibited a

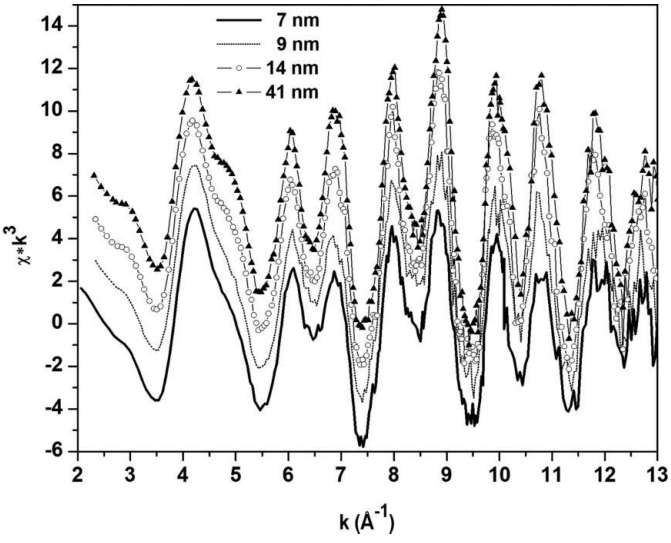

Figure 1
k^3-weighted EXAFS signal at the Zr *K*-edge corresponding to all pure ZrO_2 nanopowders studied in this work, with average crystallite sizes of 7, 9, 14 and 41 nm.

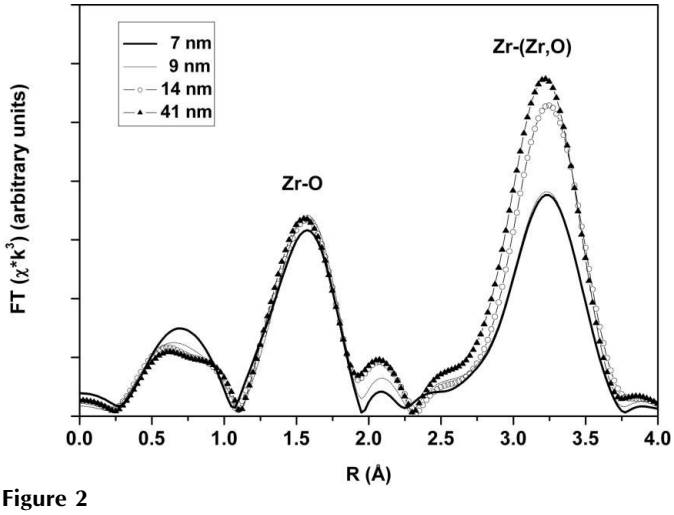

Figure 2
Fourier transforms of the EXAFS signals of Fig. 1 obtained using the *WinXas* code. The contributions of the NNs and NNNs to the EXAFS signal are identified. The peak at $R = 1.50$ Å corresponds to the first coordination shell of O atoms. The peak at $R = 3.25$ Å is related to the second and third coordination shells of Zr and O atoms, respectively. The peak at $R < 1$ Å has no physical meaning and is due to the low-frequency oscillation in the atomic background.

Table 4
Fitting parameters obtained assuming different models for the local atomic structure of tetragonal pure ZrO_2 nanopowders and using experimental amplitude and phase.

Model 2: 4 + 4, $E_{01} = E_{02}$, $\sigma_1^2 \neq \sigma_2^2$; Model 3: $N_1 \neq N_2$, $E_{01} = E_{02}$, $\sigma_1^2 = \sigma_2^2$; Model 4: 4 + 2 + 2, $E_{01} = E_{02} = E_{03}$, $\sigma_1^2 = \sigma_2^2 = \sigma_3^2$. Parameter ρ is the *WINXAS* factor of fit quality.

		Model		
Parameter	D (nm)	2	3	4
N_i	7	4 + 4 (fixed)	4.8 (5) 1.5 (2)	4 + 2 + 2 (fixed)
	9	4 + 4 (fixed)	4.3 (4) 1.6 (2)	4 + 2 + 2 (fixed)
	14	4 + 4 (fixed)	4.3 (4) 2.1 (2)	4 + 2 + 2 (fixed)
	41	4 + 4 (fixed)	4.3 (4) 2.1 (2)	4 + 2 + 2 (fixed)
R_i (Å)	7	2.10 (1) 2.31 (1)	2.10 (1) 2.34 (1)	2.10 (1) 2.26 (1) 2.43 (1)
	9	2.11 (1) 2.33 (1)	2.11 (1) 2.34 (1)	2.10 (1) 2.24 (1) 2.44 (1)
	14	2.10 (1) 2.34 (1)	2.10 (1) 2.34 (1)	2.10 (1) 2.26 (1) 2.43 (1)
	41	2.10 (1) 2.34 (1)	2.10 (1) 2.34 (1)	2.10 (1) 2.26 (1) 2.43 (1)
σ_i^2 (10^{-3}Å^2)	7	3.2 (3) 22 (2)	4.0 (4)	1.6 (2)
	9	2.5 (3) 19 (2)	2.4 (2)	2.9 (3)
	14	1.9 (2) 13 (1)	2.0 (2)	1.6 (2)
	41	1.9 (2) 13 (1)	2.1 (2)	1.6 (2)
E_{0i} (eV)	7	0 (1)	0 (1)	1 (1)
	9	1 (1)	0 (1)	1 (1)
	14	1 (1)	0 (1)	1 (1)
	41	1 (1)	0 (1)	1 (1)
ρ	7	6.0	5.4	10
	9	8.4	5.6	12
	14	8.4	5.5	10
	41	8.7	6.3	10

very good quality of fit to the experimental EXAFS signal, much better than Model 1. The results corresponding to Model 3 yielded a 4 + 2 coordination of Zr atoms ($N_1 \simeq 4$, $N_2 \simeq 2$), similar to the results from previous investigations of ZrO_2–CeO_2 and other ZrO_2-based solid solutions (Vlaic *et al.*, 1999; Fornasiero *et al.*, 1999; Kriventsov *et al.*, 2001; Fábregas *et al.*, 2008). Finally, in Model 4, we assumed a 4 + 2 + 2 coordination of O atoms around Zr ($\sigma_1^2 = \sigma_2^2 = \sigma_3^2$; $E_{01} = E_{02} = E_{03}$).

All results obtained in the present study using scattering amplitudes and phase shifts derived from the experimental standard are summarized in Table 4. The k-weighted contribution to the Zr K-edge EXAFS signal for the Zr first neighbor oxygen shell corresponding to the sample with a crystallite size of 9 nm and the fits obtained using experimental amplitude and phase assuming the models described above are displayed in Fig. 3, as an example of the quality of the achieved fits.

The results obtained using theoretical calculations with the *FEFFIT* code, summarized in Table 5, were very similar to those determined with the experimental standard discussed in the previous paragraph. The same models used for the analysis with the experimental standard were tested. Again, Model 1 gave a very poor goodness of fit for all studied samples. Conversely, Models 2, 3 and 4 provided good fits, with similar

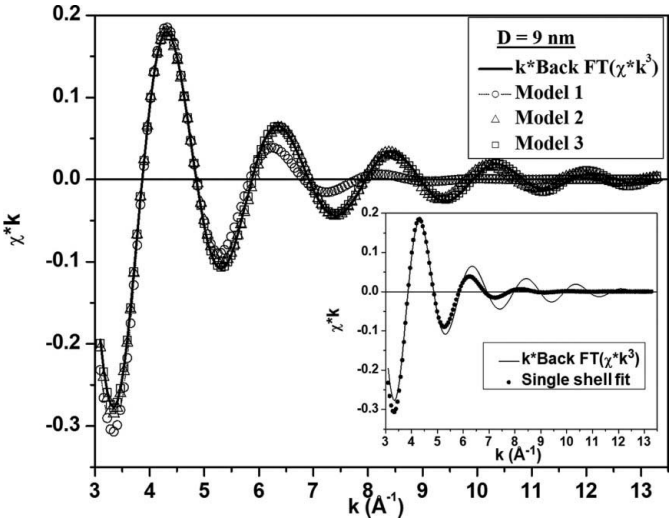

Figure 3
Fit of the k-weighted contribution to the Zr K-edge EXAFS signal for the first neighbor oxygen shell of ZrO_2 with a 9 nm crystallite size. While Models 2 and 3 (4 + 4 and 4 + 2, respectively) gave a similar quality of fit, the crystallographic model (Model 1) does not fit to the back Fourier transform of the experimental data. The inset shows a fit of the back FT assuming a single shell of eight O atoms. Fits were performed using experimental amplitude and phase.

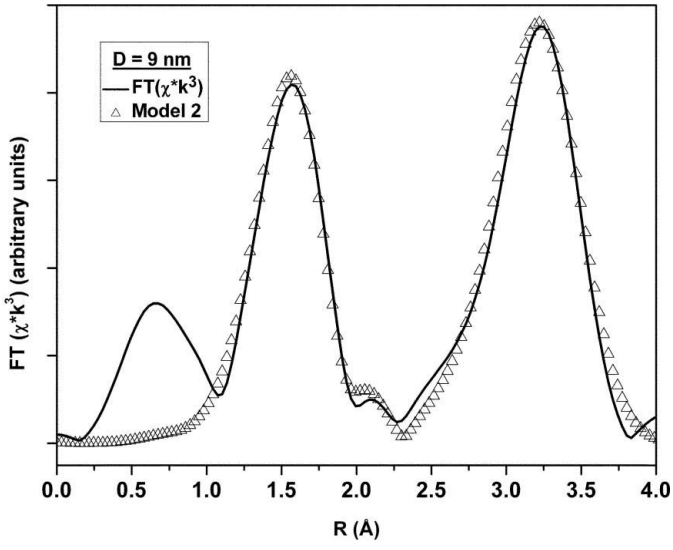

Figure 4
Fourier transform of the Zr K-edge EXAFS signal of ZrO_2 with a crystallite size of 9 nm and the fit obtained with Model 2. The fit was performed between $R = 1.20$ Å and $R = 3.80$ Å, using a theoretical model determined by the *FEFFIT* code.

Table 5
Fitting parameters obtained assuming different models for the local atomic structure of tetragonal pure ZrO_2 nanopowders and using theoretical amplitude and phase.

Model 2: 4 + 4, $E_{01} = E_{02}$, $\sigma_1^2 \neq \sigma_2^2$; Model 3: $N_1 \neq N_2$, $E_{01} = E_{02}$, $\sigma_1^2 = \sigma_2^2$; Model 4: 4 + 2 + 2, $E_{01} = E_{02} = E_{03}$, $\sigma_1^2 = \sigma_2^2 = \sigma_3^2$. Parameter r is the *FEFFIT* factor of fit quality.

		Model		
Parameter	D (nm)	2	3	4
N_i	7	4 + 4 (fixed)	4.1 (4) 1.5 (2)	4 + 2 + 2 (fixed)
	9	4 + 4 (fixed)	4.1 (4) 1.6 (2)	4 + 2 + 2 (fixed)
	14	4 + 4 (fixed)	4.7 (5) 2.1 (2)	4 + 2 + 2 (fixed)
	41	4 + 4 (fixed)	4.6 (5) 1.9 (2)	4 + 2 + 2 (fixed)
R_i (Å)	7	2.09 (2) 2.29 (4)	2.08 (3) 2.26 (6)	2.09 (2) 2.23 (2) 2.37 (1)
	9	2.10 (2) 2.28 (4)	2.09 (2) 2.29 (5)	2.09 (2) 2.24 (1) 2.37 (3)
	14	2.09 (2) 2.30 (3)	2.10 (2) 2.32 (3)	2.09 (3) 2.262 (9) 2.40 (2)
	41	2.09 (2) 2.32 (2)	2.08 (2) 2.31 (3)	2.09 (2) 2.26 (4) 2.39 (2)
σ_i^2 (10^{-3}Å^2)	7	6 (1) 17 (8)	5 (3)	5 (1)
	9	4.2 (1) 12 (5)	4 (3)	4 (2)
	14	4 (1) 11 (4)	5 (2)	4.1 (8)
	41	4.2 (8) 12 (3)	5 (2)	3.7 (6)
E_{0i} (eV)	7	1 (1)	−1 (1)	1 (3)
	9	1 (2)	−1 (1)	0 (1)
	14	1 (1)	0 (1)	1 (1)
	41	1 (1)	−1 (1)	1 (1)
r	7	0.033	0.024	0.044
	9	0.035	0.031	0.049
	14	0.019	0.019	0.027
	41	0.013	0.010	0.018

quality parameters (r factors). For example, Fig. 4 shows the fit quality in R space obtained assuming Model 2 for the sample with a crystallite size of 9 nm, where a very good agreement between data and model is clear.

Since, according to Model 2, the two oxygen subshells are very close for samples with crystallite sizes of 7 and 9 nm, we also performed additional tests using a model that assumes a single first neighbor oxygen shell with $N_1 = 8$ (crystallographic model for the cubic phase). However, the quality of the EXAFS data fit was very poor and similar to that obtained using Model 1. Therefore, this model for the local atomic arrangement was discarded. The inset in Fig. 3 shows the poor quality of fit with this $N = 8$ model.

As mentioned in §2, for the analysis using theoretical amplitudes and phases, we considered the NNs and NNNs to Zr. The results obtained for the NNNs are summarized in

Table 6
Fitting parameters of the second coordination shell of Zr, obtained assuming different models for the local atomic structure for the first Zr—O coordination shell of tetragonal pure ZrO_2 nanopowders, and using theoretical amplitude and phase.

Model 2: 4 + 4, $E_{01} = E_{02}$, $\sigma_1^2 \neq \sigma_2^2$; Model 3: $N_1 \neq N_2$, $E_{01} = E_{02}$, $\sigma_1^2 = \sigma_2^2$; Model 4: 4 + 2 + 2, $E_{01} = E_{02} = E_{03}$, $\sigma_1^2 = \sigma_2^2 = \sigma_3^2$. Parameter r is the factor of fit quality. In all cases, it was assumed that 12 NNNs are present at the same distances. Note that the results obtained for the second coordination shell are independent of the fitting model proposed for the first shell.

		Model		
	D (nm)	2	3	4
R_4 (Å)	7	3.63 (2)	3.63 (1)	3.63 (2)
	9	3.62 (2)	3.62 (2)	3.62 (2)
	14	3.63 (1)	3.63 (1)	3.63 (1)
	41	3.612 (9)	3.612 (8)	3.61 (1)
σ_4^2 (10^{-3}Å^2)	7	11.8 (7)	11.8 (6)	11.8 (8)
	9	11.7 (7)	11.7 (7)	11.7 (9)
	14	9.5 (5)	9.5 (5)	9.5 (6)
	41	8.9 (4)	9.0 (4)	9.0 (5)
E_{04} (eV)	7	3 (2)	3 (2)	2 (2)
	9	1 (2)	1 (2)	1 (2)
	14	2 (2)	2 (2)	2 (2)
	41	0 (1)	0 (1)	0 (2)
r	7	0.033	0.024	0.044
	9	0.035	0.031	0.049
	14	0.019	0.019	0.027
	41	0.013	0.010	0.018

Table 6. For Models 2, 3 and 4, the average Zr—Zr distance ranged from 3.61 to 3.64 Å, in agreement with the average distance calculated from SR-XRD data. As expected, the DW parameter of the second shell, σ_2^2, decreases with increasing crystallite size.

4. General discussion

4.1. Model 1 (N = 8)

As described in the previous section, Model 1 corresponds to the crystal structure widely accepted for the tetragonal phase: Zr atoms surrounded by eight O atoms in two subshells with the same number of O atoms ($N_1 = N_2 = 4$), and equivalent DW parameters ($\sigma_1^2 = \sigma_2^2$) and threshold electron energy shifts ($E_{01} = E_{02}$).

The plots displayed in Fig. 3 clearly show a very poor agreement between the EXAFS signal calculated from Model 1 and the experimental EXAFS data. This result indicates that the crystallographic model of the tetragonal phase is not adequate to describe the local atomic structure of the pure ZrO_2 nanomaterials studied here and thus it can be safely discarded.

4.2. Model 2 (N_1 = 4, N_2 = 4; $\sigma_1 \neq \sigma_2$)

The fitting of the EXAFS signal determined by applying Model 2 to the experimental EXAFS data yielded a 4 + 4 first neighbor Zr—O shell, with Zr—O1 and Zr—O2 distances very similar to those previously determined by SR-XRD, for all crystallite sizes (Fig. 5). For smaller crystallites, the

agreement between experimental and theoretical results for R_1 is not as good as that obtained for R_2.

The difference between the two Zr—O distances calculated with Model 2 decreases with decreasing crystallite size. Since this difference is expected to vanish for a cubic structure, this result is consistent with the proposed existence of a tetragonal-to-cubic phase transition as the crystallite size decreases, previously reported by Tsunekawa *et al.* (2003). These authors determined a critical crystallite size for the tetragonal–cubic phase boundary of about 2 nm. In fact, we also found a similar trend with decreasing crystallite size in a previous work (Lamas *et al.*, 2006).

As reported in Table 4 – results derived from the best fitting procedure by using experimental amplitudes and phases – the DW parameters, σ_1^2 and σ_1^2, corresponding to the first and second oxygen subshells, respectively, are very different: $\sigma_1^2 = 0.0032$ Å^2 and $\sigma_2^2 = 0.022$ Å^2. A similar trend for σ_1^2 and σ_2^2 is observed for the alternative fitting procedure by applying theoretical amplitude and phases (Table 5). This result is *a priori* unexpected because, according to the known crystallographic structure of the tetragonal phase, both oxygen subshells around Zr atoms are expected to have the same DW parameter. As a matter of fact, in the tetragonal structure, the second neighbor from a Zr atom, within the first shell, is the closest neighbor around Zr in the next cell. Therefore, *a priori*, those atoms should have the same crystallographic DW parameter. However, we have noticed that the conclusions of Li *et al.* (1993*c*) agree with our results. These authors studied tetragonal Y_2O_3-doped ZrO_2 solid solutions and, by proposing Model 2 for the first shell, they obtained Debye–Waller parameters corresponding to second neighbor O atoms one order of magnitude larger than those of the closest oxygen neighbors. As pointed out by the authors, the difference in the DW parameters of these two first oxygen subshells can be understood considering that O atoms can be displaced not only in the [00±1] directions, as expected for the tetragonal distortion, but also along the [±100]/[0±10] directions. It is worth mentioning that Li *et al.* (1993*c*) studied their samples at different temperatures and demonstrated that the difference between the two DW parameters can be assigned to a static distortion of the oxygen sublattice, regardless of the existence of a strong thermal effect. Taking into account that the DW parameters determined by Li *et al.* (1993*c*) at room temperature are very similar to the values determined in our work (Table 5), we have assumed that the same static distortion of the oxygen sublattice also occurs in pure ZrO_2.

The possible displacements of O atoms along the [±100]/[0±10] directions are schematically displayed in Fig. 6(*a*). This type of displacement causes an important increase in σ_2^2 since a strong change in d_2 distance is produced, while σ_1^2 remains at a low value because the variation in d_1 distance is much smaller. If the O atom is displaced a certain fixed distance δ (which will be assumed small, $\delta/a < 0.1$), this atom is no longer placed in an equivalent 4*d* site of the tetragonal phase. This operation keeps d_1 almost fixed, but it gives rise to a distinction between the two Zr—O2 bonds, as shown in Fig. 6(*b*): d_2' is shorter than its value in the 4 + 4 model (Model 2) and d_3' elongates, originating the 4 + 2 + 2 model (Model 4). In order to compare our structure models and those proposed by Li *et al.* (1993*a*,*b*,*c*, 1994), it is important to observe that these

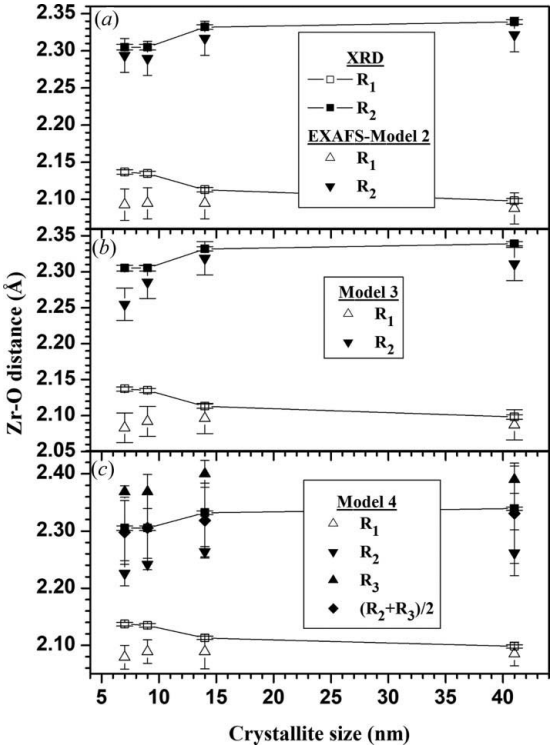

Figure 5
Comparison between Zr—O distances determined by SR-XPD and those obtained by EXAFS analysis using experimental phase and amplitude and also assuming different theoretical models for the local atomic order around Zr: (*a*) 4 + 4 coordination (Model 2); (*b*) 4 + 2 (Model 3) and (*c*) 4 + 2 + 2 (Model 4).

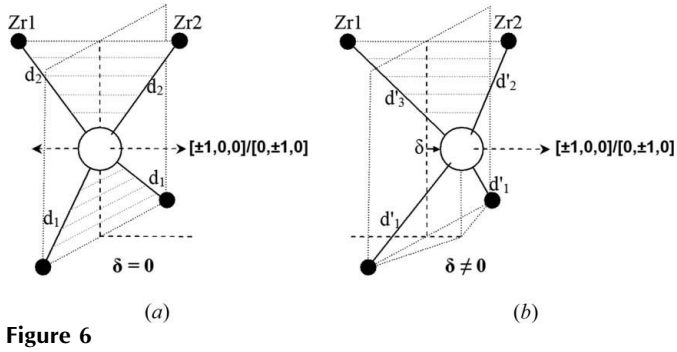

Figure 6
Model for the displacement of the O atoms that explains a more disordered second oxygen subshell around the Zr atoms. Black spheres: Zr atoms; white spheres: O atoms; δ: displacement along the [±100]/[0±10] directions (referred to the pseudo-fluorite unit cell); d_1: Zr—O1 distance in the 4 + 4 model (Model 2); d_2: Zr—O2 distance in the 4 + 4 model (Model 2); d_1': Zr—O1 distance in the 4 + 2 + 2 model (Model 4); d_2': Zr—O2 distance in the 4 + 2 + 2 model (Model 4); d_3': Zr—O3 distance in the 4 + 2 + 2 model (Model 4). (*a*) An O atom in the 4*d* site promotes two Zr—O distances d_1 and d_2. A small random displacement in the [±100]/[0±10] directions increases σ_2^2 with no significant change in σ_1^2. (*b*) A small displacement in the [±100]/[0±10] directions gives rise to three Zr—O distances, with four O atoms at d_1', two at d_2' and two at d_3' from the central Zr atom, resulting in the 4 + 2 + 2 model. See text for further explanation.

authors have used a conventional Teufer unit cell (Lee & Rainforth, 1994; Juárez *et al.*, 1999), while we have preferred to use a pseudo-cubic unit cell.

As described by Li *et al.* (1993*a*), the contribution of the second oxygen distance to the EXAFS signal is relevant only in the low-k region and it is to a large extent out of phase with the contribution of the first oxygen distance (Fábregas *et al.*, 2008). Therefore, one can expect that it would be very difficult to perceive the contribution from these long-distance O atoms in nanocrystalline samples by inspection of the associated FTs. Indeed, very small changes were observed in the amplitude of the FTs of the different samples in the range between 1.1 and 1.9 Å, as shown in Fig. 2. On the other hand, the small band between 1.9 and 2.3 Å is the only signature of these long-distance O atoms; this band presents a significant variation with crystallite size and can be used to guide the goodness of fit.

4.3. Model 3 (N_1, N_2 free; $\sigma_1 = \sigma_2$)

Previous studies of the local atomic order of nanocrystalline ZrO_2–CeO_2 solid solutions for samples with average crystallite sizes between 8 and 20 nm (Fábregas *et al.*, 2006) established a sevenfold coordination of Zr atoms over a wide range of compositions, from 15 to 80 mol% CeO_2. In these investigations, Model 3 was applied and a good agreement between SR-XRD and EXAFS results was obtained. The addition of Ce introduces important distortions in the local order of the Zr atom, due to the difference between the ionic radii of Zr^{4+} and Ce^{4+} (0.89 and 1.01 Å, respectively). Even for rather low Ce concentration, the incorporation of Ce significantly affects the average Zr—O2 distance R_2, which is enlarged from 2.30 Å in pure ZrO_2 to 2.37 Å for ZrO_2–15 mol% CeO_2. This may be the reason why the coordination number of the Zr atom in ZrO_2–CeO_2 differs from those that we have determined in the present work for pure ZrO_2. These large distortions may cause important variations in the phase of the photoelectrons scattered by different O atoms (Fábregas *et al.*, 2008), causing destructive interference effects among them and preventing the precise determination of the real distribution and number of O atoms around Zr.

More recently, we also studied the local atomic structure of ZrO_2–CaO solid solutions with compositions from 4 to 16 mol% CaO (Fábregas *et al.*, 2008). Model 3 was proposed for all compositions, yielding in all cases a good quality of fit and Zr—O distances in good agreement with those determined by SR-XRD. Model 3 applied to tetragonal ZrO_2–CaO leads to a 4 + 2 coordination of O atoms for all compositions. This agrees with the results of the same Model 3 applied to pure ZrO_2 obtained in the present investigation (Tables 4 and 5), which also lead to a good fit of EXAFS data. Unfortunately, in the case of ZrO_2–CaO solid solutions, Models 2 and 3 yielded very similar quality fits and the cation–oxygen distances agree with those determined by SR-XRD. Therefore, we could not establish a unique model to describe the corresponding local atomic order. The same situation occurs in the present study on pure ZrO_2: both models gave similar Zr—O distances and the slight improvement in the quality of fit parameter found for Model 3 may not be significant because there are more parameters in the fit procedure using Model 3 than in the fit using Model 2.

On the other hand, it is important to point out that the coordination of Zr atoms according to the crystallographic structure of tetragonal ZrO_2-based materials observed by diffraction experiments is eightfold, in contrast to the EXAFS results of Model 3, which indicated a sixfold coordination.

4.4. Model 4 ($N_1 = 4$, $N_2 = 2$, $N_3 = 2$; $\sigma_1 = \sigma_2 = \sigma_3$)

In order to understand the disorder in the second oxygen subshell associated with Model 2, we also tested an additional model consisting of three oxygen subshells with the following conditions: $N_1 = 4$, $N_2 = 2$, $N_3 = 2$; $\sigma_1^2 = \sigma_2^2 = \sigma_3^2$; $E_{01} = E_{02} = E_{03}$. This model is similar to that proposed by Vlaic *et al.* (1999), who established a 4 + 2 + 2 local atomic structure around the Zr atoms in tetragonal ZrO_2–20 mol% CeO_2 solid solutions. However, these authors supposed that the Zr—O3 distance R_3 was larger than 2.6 Å, and we found R_3 to be between 2.33 and 2.40 Å.

This model led to good quality fits of the EXAFS data for all crystallite sizes, similar to those obtained by Models 2 and 3. The average R_2 and R_3 distances, related to the second and third subshells, agree with the longest Zr—O distance determined by SR-XRD, while R_1 (first subshell) agrees with the shorter Zr—O distance. Therefore, Model 4 seems also to be in good agreement with the expected long-range order. Unfortunately, we cannot safely differentiate between (i) a broadened peak for the longer bond (Model 2) and (ii) replacing this peak with two narrower peaks, split by a distance of about 0.15 Å (Model 4).

4.5. Other models

In order to further investigate the observed disorder in the oxygen displacements or the eventual existence of more than two oxygen subshells, we also tested (1) a mixture of two tetragonal phases and (2) a mixture of tetragonal and cubic phases. Even though these models lead to EXAFS signals that also fit the experimental data, with reasonable values of R_i, σ_i^2 and E_{0i}, the SR-XRD patterns did not show any evidence of a mixture of phases. However, these alternative models should not be discarded in the case of the samples with very small crystallite size (7 and 9 nm in this work), since broadening of SR-XRD peaks may prevent the detection of phase mixtures.

4.6. Comparison of different models

The present EXAFS analysis indicates that the local atomic structure around Zr in tetragonal ZrO_2 nanopowders stabilized at room temperature can be well described by Model 2, *i.e.* a 4 + 4 first oxygen coordination shell. The distances from the Zr atoms to the first neighbor oxygen subshell range from 2.087 to 2.095 Å and to the second oxygen subshell from 2.29 to 2.32 Å.

The oxygen coordination associated with Model 2 agrees well with that expected according to the widely accepted

crystal structure of the tetragonal phase, determined from diffraction experiments by several authors. Model 2 also yields Zr—O distances similar to those independently determined from our SR-XRD data. In addition, the difference between the two Zr—O distances decreases with decreasing crystallite size, thus suggesting the existence of a boundary between the tetragonal phase and the cubic phase for a critical radius $R <$ 7 nm, as was concluded in a previous SR-XRD study (Lamas *et al.*, 2006). The best fit of the EXAFS signal derived from this 4 + 4 model to the experimental EXAFS signals yielded a DW parameter for the second oxygen subshell much larger than that for O atoms in the first subshell. As has been explained above, this feature could come from random oxygen displacements in the [±100]/[0±10] directions, a model proposed by Li *et al.* (1993*c*) for tetragonal Y_2O_3-doped ZrO_2.

Fits using Model 3 showed that a 4 + 2 coordination of Zr atoms also adjusts the EXAFS data. However, this model does not agree with the known crystallographic structure of tetragonal ZrO_2, and therefore it can be discarded. It should be pointed out that the 4 + 2 model has been previously applied to describe the local structure of several ZrO_2-based solid solutions (Vlaic *et al.*, 1999; Fornasiero *et al.*, 1999; Kriventsov *et al.*, 2001; Fábregas *et al.*, 2008). This type of structure, with a first shell coordination number lower than 8, can be understood for ZrO_2-based solid solutions with a large number of oxygen vacancies introduced by dopants with cations of lower valence than Zr (4+), but not for pure ZrO_2 nanocrystals like those studied in the present work.

An alternative explanation for the large disorder of the second oxygen subshell in Model 2 is the splitting of the second oxygen distance into two subshells with two O atoms in each of them (Model 4). As is shown in Fig. 6(*b*), this type of distortion can arise if O atoms are displaced a certain fixed distance δ in the [±100]/[0±10] directions. Assuming this model, we have determined that the longest Zr—O distance R_3 ranges from 2.37 to 2.40 Å, while the intermediate Zr—O distance R_2 is within 2.23–2.26 Å and the shortest distance R_1 is within 2.080–2.094 Å. The value of the average of the R_2 and R_3 distances agrees with the second Zr—O2 distance within the first shell determined from SR-XRD data, and the Zr—O1 distances determined by the two techniques are also very similar. Therefore, by considering non-symmetric d displacements perpendicular to the **z** direction, the Zr—O distances calculated with EXAFS and XRD data can be correctly understood and meaningfully compared.

Model 4 can be seen as a special case of Model 2. As a matter of fact, the second subshell containing four O atoms and presenting a high disorder (high DW parameter) in Model 2 is similar to two close oxygen (2 + 2) subshells, each of them having a small DW parameter in Model 4. Thus the average spatial distribution of oxygen around the Zr atoms is similar in Models 2 and 4.

It is also worth noticing that we have obtained similar results for all samples analyzed in this work, synthesized by different routes and with different average crystallite sizes. For this reason, we can safely affirm that our conclusions are not related to eventual surface effects.

Even though several previous EXAFS studies on ZrO_2-based materials have been published, to our knowledge, there are no other papers reporting a systematic and comparative analysis of tetragonal pure ZrO_2. Our EXAFS study clearly demonstrates that the crystallographic structure widely accepted for the tetragonal phase, comprising two oxygen subshells around the Zr atoms with (i) 4 + 4 coordination and (ii) equivalent DW parameters for both subshells, is not adequate to describe the local atomic structure around Zr atoms in nanocrystalline and pure ZrO_2 materials.

5. Conclusions

We have applied the EXAFS technique to analyze the local atomic order in nanocrystalline pure ZrO_2 powders exhibiting the tetragonal phase and with different average crystallite sizes. In order to establish a consistent model for the Zr—O bonding in agreement with the crystallographic structure generally accepted for the tetragonal phase, several local atomic arrangements or local structure models were proposed and compared with those previously determined from SR-XRD experiments.

Compatible with the generally accepted average structure derived from crystallographic analysis, we have concluded that the local structure around the Zr atom in ZrO_2 nanocrystals can be well described by a model consisting of two subshells with four O atoms each (Model 2). In accordance with previous results (Lamas *et al.*, 2006), the difference between the two Zr—O distances decreases with decreasing crystallite size. On the other hand, as qualitatively expected, the DW parameters increase with decreasing average crystallite size. We have determined a rather large DW parameter for the second oxygen subshell that is not consistent with what is expected from the known crystallographic structure. However this result can be understood as an effect of oxygen displacements along the [±100]/[0±10] directions, as Li *et al.* (1993*c*) proposed for tetragonal Y_2O_3-doped ZrO_2 solid solutions. Interestingly, our EXAFS study presented here for pure (undoped) ZrO_2 demonstrates that this distortion is not necessarily related to the presence of dopant cations as in the ZrO_2-based solid solutions studied by Li *et al.* (1993*c*).

We have also proposed an alternative 4 + 2 + 2 model for the first oxygen shell around the Zr atoms with the same DW parameters for the three oxygen subshells. This model gave approximately the same factor of fit quality as Model 2 (4 + 4). In addition, both local structures are in good agreement with the crystallographic structure determined by X-ray diffraction. Even though we cannot differentiate between the two models from fit quality criteria, the 4 + 2 + 2 model with equivalent DW parameters can be considered as a particular case of the previously discussed 4 + 4 model with different DW parameters.

Very similar results regarding the local order in tetragonal pure ZrO_2 nanopowders were obtained for all of the studied samples, despite the fact that they were synthesized through different routes and thus had different average crystallite sizes (from 7 up to 41 nm). This corroborates the robustness of our

conclusion about the relevant features of the local structural model proposed in this work.

The present work was performed within the frame of the scientific collaboration agreements CAPES–MinCyT and CNPq–CONICET between Brazil and Argentina. It was also partially supported by LNLS (Brazilian Synchrotron Light Laboratory, Brazil (proposals D04B-XAFS1-4204, D10B-XPD-4276 and D04B-XAFS1-7248), CNPq (Brazil, Prosul projects 490289/2005-3 and 490580/2008-4), Agencia Nacional de Promoción Científica y Tecnológica (Argentina, PICT 2005 No. 38309 and PICT 2007 No. 01152), CONICET (Argentina, PIP No. 6559) and the Latin-American Centre for Physics (CLAF). LMA and IOF thank Fundación YPF for PhD fellowships. The authors thank A. Fernández (CITEFA, Argentina) for the synthesis of the sol-gel sample.

References

Ankudinov, A. L., Ravel, B., Rehr, J. J. & Conradson, S. D. (1998). *Phys. Rev. B*, **58**, 7565–7576.

Chadwick, A. V., Mountjoy, G., Nield, V. M., Poplett, I. J. F., Smith, M. E., Strange, J. H. & Tucker, M. G. (2001). *Chem. Mater.* **13**, 1219–1229.

Fábregas, I. O., Fuentes, R. O., Lamas, D. G., Fernández de Rapp, M. E., Walsöe de Reca, N. E., Fantini, M. C. A., Craievich, A. F., Prado, R. J., Millen, R. P. & Temperini, M. L. A. (2006). *J. Phys. Condens. Matter*, **18**, 7863–7881.

Fábregas, I. O., Lamas, D. G., Walsöe de Reca, N. E., Fantini, M. C. A., Craievich, A. F. & Prado, R. J. (2008). *J. Appl. Cryst.* **41**, 680–689.

Ferreira, F. F., Granado, E., Carvalho, W. Jr, Kycia, S. W., Bruno, D. & Droppa, R. Jr (2006). *J. Synchrotron Rad.* **13**, 46–53.

Fornasiero, P., Fonda, E., Di Monte, R., Vlaic, G., Kaspar, J. & Graziani, M. (1999). *J. Catal.* **187**, 177–185.

Garvie, R. C. (1965). *J. Phys. Chem.* **69**, 1238–1243.

Garvie, R. C. (1978). *J. Phys. Chem.* **82**, 218–224.

Garvie, R. C., Hannink, R. H. J. & Pascoe, R. T. (1975). *Nature* (*London*), **258**, 703–705.

Juárez, R. E., Lamas, D. G., Lascalea, G. E. & Walsöe de Reca, N. E. (1999). *Defect Diffus. Forum*, **177**, 1–26.

Koningsberger, D. C. & Prins, R. (1988). *X-ray Absorption: Principles, Applications, Techniques of EXAFS, SEXAFS and XANES.* New York: John Wiley & Sons.

Kriventsov, V., Kochubey, D., Navio, J. A., Hidalgo, M. C., Colón, G., Tsodikov, M., Maksimov, Y. & Suzdalev, I. (2001). *J. Synchrotron Rad.* **8**, 528–530.

Lamas, D. G., Fuentes, R. O., Fábregas, I. O., Fernández de Rapp, M. E., Lascalea, G. E., Casanova, J. R., Walsöe de Reca, N. E. & Craievich, A. F. (2005). *J. Appl. Cryst.* **38**, 867–873.

Lamas, D. G., Rosso, A. M., Suarez Anzorena, M., Fernández, A., Bellino, M. G., Cabezas, M. D., Walsöe de Reca, N. E. & Craievich, A. F. (2006). *Scr. Mater.* **55**, 553–556.

Lascalea, G. E., Lamas, D. G., Djurado, E. & Walsöe de Reca, N. E. (2001). Proceedings of 22nd Risø International Symposium on Materials Science, Risø National Laboratory, Roskilde, Denmark, pp. 313–318.

Lee, P. A., Citrin, P. H., Eisenberger, P. & Kincaid, B. M. (1981). *Rev. Mod. Phys.* **53**, 769–806.

Lee, W. E. & Rainforth, W. M. (1994). *Ceramic Microstructures: Property Control by Processing*, p. 317. London: Chapman and Hall.

Lemaux, S., Bensaddik, A., van der Eerden, A. M. J., Bitter, J. H. & Koningsberger, D. C. (2001). *J. Phys. Chem. B*, **105**, 4810–4815.

Li, P., Chen, I.-W. & Penner-Hahn, J. E. (1993*a*). *Phys. Rev. B*, **48**, 10063–10074.

Li, P., Chen, I.-W. & Penner-Hahn, J. E. (1993*b*). *Phys. Rev. B*, **48**, 10074–10081.

Li, P., Chen, I.-W. & Penner-Hahn, J. E. (1993*c*). *Phys. Rev. B*, **48**, 10082–10089.

Li, P., Chen, I.-W. & Penner-Hahn, J. E. (1994). *J. Am. Ceram. Soc.* **77**, 1281–1288.

Newville, M., Ravel, B., Haskel, D., Rehr, J. J., Stern, E. A. & Yacoby, Y. (1995). *Physica B*, **208–209**, 154–156.

Nowotny, J. (1994). *Science of Ceramic Interfaces II.* Amsterdam: Elsevier Science.

Ressler, T. (1998). *J. Synchrotron Rad.* **5**, 118–122.

Tolentino, H., Cezar, J. C., Cruz, D. Z., Compagnon-Cailhol, V., Tamura, E. & Martins Alves, M. C. (1998). *J. Synchrotron Rad.* **5**, 521–523.

Tsunekawa, S., Ito, S., Kawazoe, Y. & Wang, J. T. (2003). *Nano Lett.* **3**, 871–875.

Vlaic, G., Di Monte, R., Fornasiero, P., Fonda, E., Kaspar, J. & Graziani, M. (1999). *J. Catal.* **182**, 378–389.